

Far-Field Drag Analysis of NASA Common Research Model Simulations by JAXA

Makoto Ueno*, Kazuomi Yamamoto†, Kentaro Tanaka‡ and Mitsuhiro Murayama§

Japan Aerospace Exploration Agency, Chofu, Tokyo, 182-8522, Japan

Renato Tognaccini¶

Università degli Studi di Napoli "Federico II", Napoli, 80125, Italy

Far-field drag analysis was performed on computational fluid dynamics simulation results of the NASA Common Research Model performed in JAXA for the Drag Prediction Workshop 4. Three levels of grid were employed in that simulation and the far-field analysis successfully acquired close values to the converged drag value estimated by near-field analysis of convergence study for all levels of grid. Drag decomposition in far-field analysis also revealed which part of the flow and which component of the drag varies for variation of angle of attack. The visualized images of drag production were got from the far-field analysis and they gave good insight of production of drag.

I. Introduction

DRAG prediction employing computational fluid dynamics (CFD) is recently getting a lot of remarks and the AIAA drag prediction workshops have been held since 2001^{1,2,3,4} to improve its precision. The information about the workshop can be acquired from the [web page](#).

The collective results of the various attendee of the workshop are still wide spread⁵ and it is obvious that even the finest grid attainable is producing spurious drag. The spurious drag is a drag component which is produced due to the numerical (not physical) entropy production in the computational flow-field. The grid dependency depends on not only grid number but grid quality. Then, simple increase of grid number does not allow to get precise grid. To know the grid quality and to perform detailed analysis of the drag production in the computational field, the far-field approach is effective because of:

- Almost direct count of the spurious drag,^{6,7,8,9}
- Only way to obtain the decomposition into the physical components viscous, wave and lift induced,^{6,7,8,9}
- Visualization of drag production,^{8,9,10}
- Grid quality verification using visualized drag.^{11,12}

Japan Aerospace Exploration Agency (JAXA) and Università degli Studi di Napoli "Federico II" have been cooperatively developing a far-field drag analysis code named TEBUNCO since 2009 to build a concrete technology to realize easy-to-use and stable analysis because the analysis required some experiences and know-hows to detect physical drag production properly. In this articles, a far-field drag analysis was performed on the CFD results presented by JAXA at the 4th drag prediction workshop (DPW-4) using TEBUNCO. The detailed steps of the analysis and the acquired results including visualized drag production in the flow field are shown and examined.

*Associate Senior Researcher, Institute of Aerospace Technology, ueno.makoto@jaxa.jp, Senior Member AIAA.

†Senior Researcher, Aviation Program Group, yamamoto.kazuomi@jaxa.jp, Senior Member AIAA.

‡Research Engineer, Engineering Solution Division, Ryoyu Systems Co.,Ltd.

§Associate Senior Researcher, Aviation Program Group, murayama.mitsuhiro@jaxa.jp, Senior Member AIAA.

¶Associate Professor, Dipartimento di Progettazione Aeronautica, renato.tognaccini@unina.it, Senior Member AIAA.

II. Far-Field Method

The far-field drag analysis method employed in this article is based on the method of Tognaccini⁹ for viscous (profile) and wave drag and the method of Maskell¹³ refurbished by Kusunose¹⁴ for induced drag. At first, the theoretical background is briefly explained in this section.

A. Far-field Aerodynamic Force

A steady fluid flow with free-stream velocity U_∞ around an aircraft without power is considered, given the only external force acting on the body is due to the fluid. The momentum balance for a volume Ω surrounding the body allows for the following alternative definitions of the aerodynamic force acting on the body:

$$\begin{aligned} \mathbf{F} &= \int_{\partial B} \{(p - p_\infty) \mathbf{n} - (\boldsymbol{\tau} \cdot \mathbf{n})\} dS \\ &= - \int_{\Sigma} \left\{ \rho \mathbf{V} \mathbf{V}^T + (p - p_\infty) \mathbf{I} - \boldsymbol{\tau} \right\} \cdot \mathbf{n} dS \end{aligned} \quad (1)$$

where p is the static pressure, $\boldsymbol{\tau}$ is the stress vector, \mathbf{V} is the velocity vector, \mathbf{I} is the second-order unit tensor, and \mathbf{n} is the unit normal vector pointing outside the volume Ω and normal to its surface. The surface are composed of ∂B and Σ . The ∂B is the aircraft surface and Σ is the external surface bounding the volume Ω . In Eq. (1), non-slip (RANS) or tangential flow on the body walls (Euler: $\mathbf{V} \cdot \mathbf{n} = 0$ on ∂B) is assumed.

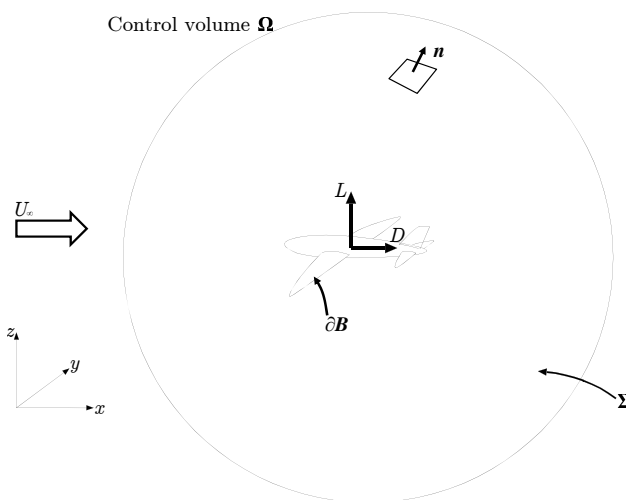


Figure 1. The control volume Ω , the body surface ∂B and external surface Σ , \mathbf{n} is directed outward of Ω .

The first representation corresponds to the well known near-field aerodynamic force. And, the second one is the far-field representation. Given the x -axis of a Cartesian system ($Oxyz$) is aligned to the free-stream velocity vector, the drag force is defined as the projection of the force \mathbf{F} on the x direction. If the far-field surface Σ is chosen sufficiently far from the body, the viscous stresses can be neglected and the far-field drag expression is acquired as follow,

$$D_{\text{far}} = - \int_{\Sigma} \{(p - p_\infty) n_x + \rho u (\mathbf{V} \cdot \mathbf{n})\} dS \quad (2)$$

When the relation $u = \hat{v}_x |\mathbf{V}|$ (where \hat{v}_x is the x -component of the unit vector specifying the direction of the velocity) is introduced, the drag equation can be written as

$$D_{\text{far}} = - \int_{\Sigma} \left\{ \rho U_\infty^2 \frac{1}{\gamma M_\infty^2} \frac{\Delta p}{p_\infty} n_x + U_\infty \hat{v}_x \frac{|\mathbf{V}|}{U_\infty} \rho (\mathbf{V} \cdot \mathbf{n}) \right\} dS \quad (3)$$

For a perfect gas, it is possible to express the module of the velocity in terms of variations of total enthalpy, $H(= H - H_\infty)$, entropy, $s(= s - s_\infty)$, and static pressure, $p(= p - p_\infty)$ (Ref.⁶):

$$\frac{|\mathbf{V}|}{U} = \sqrt{1 + 2\frac{H}{U^2} - \frac{2}{(\gamma-1)M^2} \left\{ \left(\frac{p}{p_\infty} + 1 \right)^{\frac{\gamma-1}{\gamma}} \exp \left(\frac{s}{R} \frac{\gamma-1}{\gamma} \right) - 1 \right\}} \quad (4)$$

where γ is the specific heat ratio. Hence, the drag can be expressed with the flux of $f \left(\frac{\Delta p}{p_\infty}, \frac{\Delta s}{R}, \frac{\Delta H}{U_\infty^2} \right)$ across :

$$D_{\text{far}} = -U \int_{\Sigma} \rho f \left(\frac{p}{p_\infty}, \frac{s}{R}, \frac{H}{U_\infty^2} \right) (\mathbf{V} \cdot \mathbf{n}) dS - \int_{\Sigma} \left(\rho U^2 \frac{1}{\gamma M^2} \frac{p}{p_\infty} n_x \right) dS \quad (5)$$

Equation 4 can be expanded in Taylor series obtaining

$$\begin{aligned} \frac{|\mathbf{V}|}{U} = & 1 + c_{p1} \frac{p}{p_\infty} + c_{s1} \frac{s}{R} + c_{H1} \frac{H}{U_\infty^2} \\ & + c_{p2} \left(\frac{p}{p_\infty} \right)^2 + c_{s2} \left(\frac{s}{R} \right)^2 + c_{H2} \left(\frac{H}{U_\infty^2} \right)^2 \\ & + c_{ps2} \left(\frac{p}{p_\infty} \right) \left(\frac{s}{R} \right) + c_{pH2} \left(\frac{p}{p_\infty} \right) \left(\frac{H}{U_\infty^2} \right) \\ & + c_{sH2} \left(\frac{s}{R} \right) \left(\frac{H}{U_\infty^2} \right) \\ & + O \left(\left(\frac{p}{p_\infty} \right)^3, \left(\frac{s}{R} \right)^3, \left(\frac{H}{U_\infty^2} \right)^3 \right) \end{aligned} \quad (6)$$

where the coefficients are determined as follows,

$$c_{p1} = -\frac{1}{\gamma M^2}, \quad c_{s1} = -\frac{1}{\gamma M^2}, \quad c_{H1} = 1 \quad (\text{1st order coefficient}) \quad (7)$$

$$c_{p2} = -\frac{1 - M^2}{2\gamma^2 M^4}, \quad c_{s2} = -\frac{1 + (\gamma - 1) M^2}{2\gamma^2 M^4}, \quad c_{H2} = -\frac{1}{2} \quad (\text{2nd order coefficient}) \quad (8)$$

$$c_{ps2} = -\frac{1 + (\gamma - 1) M^2}{\gamma^2 M^4}, \quad f_{pH2} = \frac{1}{\gamma M^2}, \quad f_{sH2} = \frac{1}{\gamma M^2} \quad (\text{cross term}) \quad (9)$$

Thus, after substitution of series expansion Eq. 6 into Eq. 5, the far-field drag can be written as

$$\begin{aligned} D_{\text{far}} = & -U \int_{\Sigma} \hat{v}_x \left\{ c_{s1} \frac{s}{R} + c_{s2} \left(\frac{s}{R} \right)^2 \right\} \rho (\mathbf{V} \cdot \mathbf{n}) dS \\ & - U \int_{\Sigma} \hat{v}_x \left\{ c_{H1} \frac{H}{U_\infty^2} + c_{H2} \left(\frac{H}{U_\infty^2} \right)^2 \right\} \rho (\mathbf{V} \cdot \mathbf{n}) dS \\ & - U \int_{\Sigma} \hat{v}_x \left\{ 1 + c_{p1} \frac{p}{p_\infty} + c_{p2} \left(\frac{p}{p_\infty} \right)^2 \right\} \rho (\mathbf{V} \cdot \mathbf{n}) dS \\ & - \rho U^2 \frac{1}{\gamma M^2} \int_{\Sigma} \frac{p}{p_\infty} n_x dS \\ & - U \int_{\Sigma} \hat{v}_x \left\{ c_{ps2} \frac{p}{p_\infty} \frac{s}{R} + c_{pH2} \frac{p}{p_\infty} \frac{H}{U_\infty^2} + c_{sH2} \frac{s}{R} \frac{H}{U_\infty^2} \right\} \rho (\mathbf{V} \cdot \mathbf{n}) dS \\ & + O \left(\left(\frac{s}{R} \right)^3, \left(\frac{H}{U_\infty^2} \right)^3, \left(\frac{p}{p_\infty} \right)^3 \right) \end{aligned} \quad (10)$$

The first integral is related with the entropy rise s/R mainly by the boundary layers and shock waves. It is defined as the entropy drag. The second integral depends on H and it is small value generally in the power-off condition. But, it is strictly connected with thrust in the case of power-on conditions. The third

and fourth integrals are related to the pressure variations and to the angle between the local velocity vector \mathbf{V} and the free-stream direction, \hat{v}_x , which is not negligible downstream in the wake of lifting bodies. This contribution, only present in three-dimensional flows is defined as induced drag.

The contributions due to entropy production and enthalpy production in Eq. 10 can be expressed in divergence form by applying the Gauss's theorem to the vector field $\rho(\mathbf{V} \cdot \mathbf{n})$ in the finite flow domain Ω . Additionally, $\hat{v}_x \ll 1$ on the far-field boundary allows the drag components to be written as follows,

$$D_{s1} = U \int_{\Omega} \nabla \cdot \left(-c_{s1} \left(\frac{s}{R} \right) \rho \mathbf{V} \right) d\Omega \quad (11)$$

$$D_{s2} = U \int_{\Omega} \nabla \cdot \left(-c_{s2} \left(\frac{s}{R} \right)^2 \rho \mathbf{V} \right) d\Omega \quad (12)$$

$$D_{H1} = U \int_{\Omega} \nabla \cdot \left(-c_{H1} \left(\frac{H}{U^2} \right) \rho \mathbf{V} \right) d\Omega \quad (13)$$

$$D_{H2} = U \int_{\Omega} \nabla \cdot \left(-c_{H2} \left(\frac{H}{U^2} \right)^2 \rho \mathbf{V} \right) d\Omega \quad (14)$$

$$D_{sH2} = U \int_{\Omega} \nabla \cdot \left(-c_{sH2} \frac{s}{R} \frac{H}{U^2} \rho \mathbf{V} \right) d\Omega \quad (15)$$

They are 1st and 2nd order entropy drag, 1st and 2nd order enthalpy drag, and the cross term of the entropy and enthalpy. Because pressure drag (=lift induced drag) cannot be applied with the Gauss's theorem, it is omitted here. In this analysis, Shima's GLSQ¹⁵ was employed to calculate gradient.

The expressions above realize the volume integral of the drag components. Hence, provided an unique definition of the viscous (boundary layer and wake) and of the shock wave regions, the domain Ω can be decomposed as $\Omega = \Omega_v \cup \Omega_w \cup \Omega_{sp}$. Ω_v is the volume containing the boundary layer and the viscous wake, Ω_w contains the shock waves, and Ω_{sp} specifies the remaining part of the flow-field. Thus, the drag components can be decomposed into three contributions:

$$D = D_v + D_w + D_{sp} \quad (16)$$

B. Region Selection

To decompose the drag into components, cells to be integrated have to be selected as described above. The drag integration of the cells selected as the wave drag region is wave drag, and the integration of the cells selected as the boundary layer is profile drag. Remaining cells are considered to be producing spurious drag.

1. Shock Wave Region

To automatically select the shock wave region, the following so-called "shock function" is used in this analysis.

$$F_{\text{shock}} = \frac{\mathbf{V} \cdot \nabla p}{a|\nabla p|} \quad (17)$$

where a is the local sound speed.

2. Boundary-layer Region

The eddy viscosity was used as a viscous region sensor. It works well for the fully turbulent flow. The adopted sensor is

$$F_{\text{bl}} = \frac{\mu_l + \mu_t}{\mu_l} \quad (18)$$

where μ_l and μ_t are the dynamic and eddy viscosities, respectively.

C. Maskell's Induced Drag

The induced drag was computed using the method originated by Maskell.¹³ The method was improved by Kusunose¹⁴ and it was employed in this analysis.

The computational space was cut by a plane which is set at an arbitrary downstream position normal to the free-stream direction, then on that plane, vorticity and flow potential of the flow in the plane were computed and used to compute induced drag at the position. In this article, the plane defined above is called "cut plane." On the plane, 2-dimensional flow is defined and Maskell's induced drag is defined as follows,

$$D_i = \frac{\rho}{2} \iint_{W_A} \psi \xi dy dz \quad (19)$$

The subscript W_A represents the wake region on the cut plane and ξ is vorticity defined on the cut plane. In the flow downstream of the body, the vorticity is almost zero except for the wake region. In Eqn. 19, ψ is a scalar function defined on the cut plane and it is the solution of the Poisson equation

$$\frac{\partial^2 \psi}{\partial y^2} + \frac{\partial^2 \psi}{\partial z^2} = -\xi \quad (20)$$

with the boundary condition of

$$\psi = 0 \quad (21)$$

at infinity.

The volume integration of drag was performed using the cells confined to the upstream of the plane to compute the induced drag and the sum of the volume integral drag and the induced drag is the total drag.

III. Numerical Analysis Tools

A. Target Solution to be Analysed

The data used in this article was given from the numerical simulation performed by Yamamoto *et al.*¹⁶ As the flow solver, UPACS^{17,18} was used, which is a standard CFD code for multi block structured grids in Japan Aerospace Exploration Agency. The flow solver is based on a cell-centered finite volume method. In this study, the second-order scheme of Roe's flux difference splitting for convection terms¹⁹ is used with MUSCL extrapolation and van Albada's differentiable limiter.²⁰ The viscous terms are discretized by 2nd-order central difference. Time integration is carried out using MFGS (Matrix Free Gauss-Seidel) implicit method.²¹

The grid wraps around the geometry near the model surface with O-O grid topology to guarantee good orthogonality within the boundary layer, and then extends outward with C-O topology. The wire frame image of the grid blocks around the NASA CRM is shown in Fig. 2.

Three levels of grid were prepared and the detail of them are tabulated in Table 1.

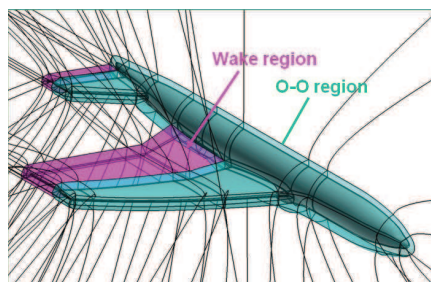


Figure 2. Block wire frame around NASA CRM model.

Table 1. Multi-block structured grid.

	Cells	Surface Faces	B.L. 1st-Cell Size [inch]	B.L. Growth Rate	T.E. Cells
Coarse*	2.8M	127K	0.001478	1.31	14
Medium	9.0M	276K	0.000985	1.20	20
Fine†	30.4M	620K	0.000657	1.13	30

* Based on interpolation of Medium grid.

† Based on interpolation of Medium grid.

Spalart-Allmaras one-equation turbulence model²² was used without the trip term for transition and the *ft2* function which intends to suppress production of eddy viscosity due to numerical error. The production of eddy viscosity starts with the free stream value.

Free-stream Mach number is $M_\infty = 0.85$ and Reynolds number is 5 million. Angles of attack α of $C_L = 0.5$ were chosen to be used for grid convergence study and $\alpha = 1.5, 2.0, 2.5, 3.0$, and 4.0 were examined only for medium grid in this analysis. The horizontal stabilizer angle was set at 0° .

B. Far-Field Drag Analysis Code

To perform far-field drag analysis, a computer program named TEBUNCO developed cooperatively by Japan Aerospace Exploration Agency and Università degli Studi di Napoli "Federico II" was used in this analysis. TEBUNCO does not depend on a specific solver and it can perform far-field drag analysis accepting a flow-field data of unstructured multi-block CFD solution written in the vertex-centered CGNS²³ format.

IV. Far-Field Drag Analysis

A. Pre-Conditioning for Profile and Wave Drag

The far-field analysis is depending on the way how to select the proper cell to be integrated. To acquire good results, some procedures are required and they are explained in this section.

1. Far-Field Boundary Margin

Along the far-field boundary of the flow-field, the entropy production distribution is contaminated by entropy oscillation due to the far-field boundary condition. As the first step of the pre-conditioning, some layers of cells from the far-field boundary should be omitted from the volume integration of entropy drag to avoid the influence of this oscillation. In the cases handled in this article, only 1-layer removal is enough.

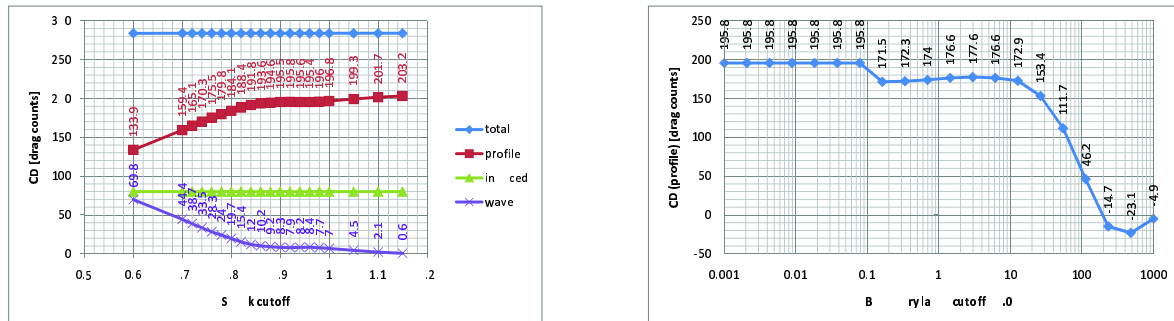
2. Cut-off Value Determination

As described in Section IV.B, the shock function (Eq. 17) and the eddy viscosity (Eq. 18) were used to select the cells to be integrated for the wave drag and the profile drag, respectively. Specifically, the cells are selected if the value of the sensor in the cell is larger than a cut-off value. To determine an appropriate sensor cut-off value, surveys changing the value of those sensors were performed. After choosing an appropriate number, it is known from experiences that the same number can be generally used for similar simulation results acquired using the same solver if the grids used are different.

In this analysis, the shock sensor was defined to have a precedence over the boundary layer sensor. In such a case, when a value is set for the boundary layer function and the shock function cut-off value are increased from very low value, boundary layer region were interchanged with shock region and the number of the selected cells as the boundary layer (profile drag) increases. Because the shock function value is proportional to the local Mach number, the lower the shock cut-off value is set, the larger number of cells would be selected. An example of such a survey is shown in Fig. 3(a). Increasing the shock function cut-off value above the free-stream Mach number, the interchange between wave drag cells and the boundary layer cells stopped and it should be a good number to choose as a shock function cut-off. In this analysis $F_{\text{shock}} = 0.92$ was chosen.

As same as the shock cut-off, boundary layer sensor should have a cut-off value. When the boundary layer sensor is set as very low value, almost entire region would be selected as boundary layer. Increasing the boundary layer sensor cut-off value, discrete change would be observed and after that the proper boundary layer region would be captured. Then, while the cut-off value was continuously increased, no cell would be selected finally. An example of such a survey for boundary layer cell detection is shown in Fig. 3(b). Because the boundary layer sensor value varies in a wide range, logarithmic scale was used for the abscissa. The value can be chosen almost anywhere between the discrete change above 0.1 and to the point around 10.0 which starts gradual decrease of captured boundary layer cells. For this analysis, $F_{bl} = 4.0$ was chosen.

Thus, appropriate values are chosen for this analysis. Practically, visual inspection would be recommended to confirm those values really capture wave drag cells and boundary layer cells.



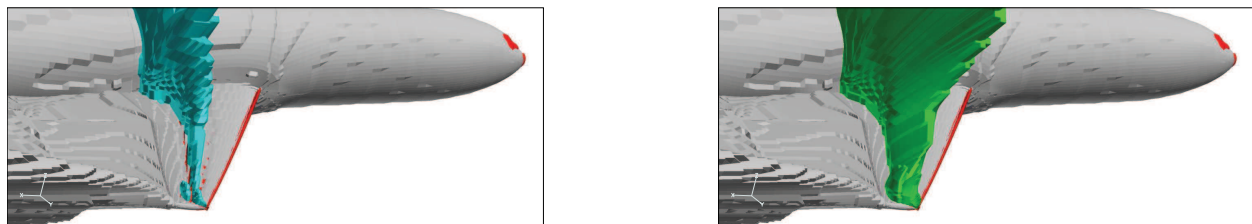
(a) Drag values variation due to shock function value.

(b) Profile drag variation due to boundary layer function value.

Figure 3. Cutoff value variation and computed drag.

3. Margins around Shock and Boundary Layer

Although the shock function and the eddy viscosity work well, those sensors cannot select the regions perfectly sometimes. For the wave drag, in many cases, the shock function cannot capture all the oscillation found around the shock due to the characteristics of the numerical scheme employed in the solver. In figure 4(a), sky blue cells represent the cells selected only with the shock function and the red cells are the missed cells. Around the wave drag cells, there are small pieces of missed wave drag especially around the tip-half of the main wing. To include those cells, margin extension of selected regions was performed in this analysis.



(a) Only with shock function.

(b) With 5-layers of margin.

Figure 4. Region selection by shock function and margin effect.

The strategy to build the margin extension is depicted in Fig. 5. It is simple and single layer of cells

adjacent to the selected region cells are selected as the 1st layer of margin extension and those layer would be stacked around the selected region one layer by one layer. With 5-layers of margins, the wave drag fractions which are missed to be captured could be included in the integration cells for the wave drag for this analysis. While the margin perhaps seems excessive, margin extension into the main flow region is usually harmless. Shock margin effect for the final integrated wave drag are 3.0, 1.6, and 0.4 drag count for the coarse, the medium and the fine grid.

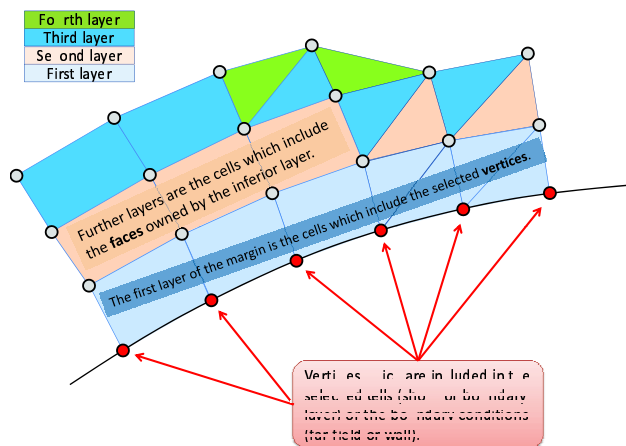
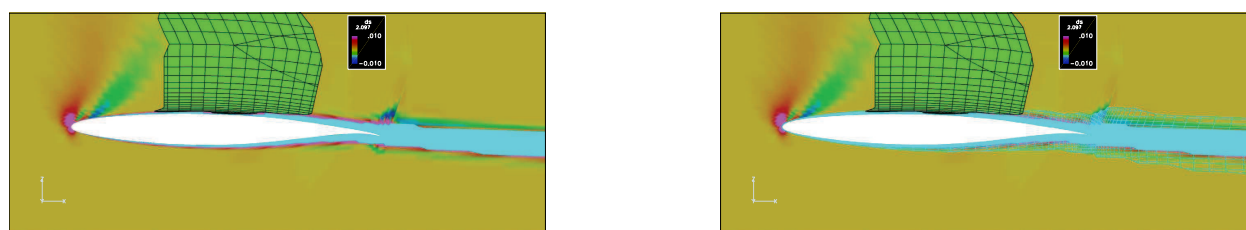


Figure 5. Margin layer building strategy

As same as the wave drag, profile drag due to entropy production within the boundary layer could have an oscillation at the edge of the boundary layer because it is a discontinuity, as well. Figure 6(a) shows that the entropy drag production around the airfoil cut at the wing section of $\eta = 0.5$. The green cells are the wave drag cells and the sky blue cells are the cells selected by the boundary layer function employing the eddy viscosity. It is obvious that especially in the aft-region and the wake, the boundary layer function could not capture all the effect produced by the boundary layer entropy production. Employing the same method to grow the margin around the boundary layer, sky blue meshed region were additionally selected and those cells are almost adequate to include all the entropy production due to the boundary layer. This boundary layer margin effect is large and they are 13.6, 6.9 and 3.2 drag counts for the coarse, the medium and the fine grid case, respectively. It means advent of more proper boundary layer detection method is waited.



(a) Only with shock function.

(b) With 2-layers of margin.

Figure 6. Region selection by boundary layer function and margin effect (coarse grid, $\eta = 0.5$).

4. Wall Margin

Eddy viscosity is very small in the region adjacent to the surface of the model. Thus, the cells very close to the model could not be captured as boundary layer by the cut-off value. To include such cells, margins which grow from the model wall were used. In this analysis, 5-, 8-, and 11-layers of wall margins for the coarse, the medium, and the fine grid were used.

B. Induced Drag

After determining the cut-off values and margins, volume integration for the wave drag and profile drag can be performed and induced drag was calculated simultaneously. Maskell's method was employed in this study to compute induced drag as described in Section II.C. The method requests a 2-dimensional flow-field on a plane which is perpendicular to the free-stream direction and is placed behind the model body without intersecting the model itself. Such flow-field was got by interpolation of the flow field. To acquire proper induced drag by Maskell's method, the outer boundary of the flow-field should be removed from the flow field data.

The induced drag computed by Maskell's method depends on the cut position of the 2-D flow-field because of the interchange between induced drag and entropy drag due to numerical dissipation in the outer flow-field.⁸ The induced drag output plotted versus the cut positions are shown in Fig. 7. In the figures, the abscissae are normalized by the reference length (MAC) of the model and the cut plane does not cut the model downstream from the normalized scale of about 10.

Excluding the position very close to the body ($x = 10$), total drag which are comprised of the profile, the wave (shock) and the induced drag are almost constant and slight interchange between the profile drag and the induced drag was observed for all levels of the grid. Some induced drag fluctuations were observed while varying the cut plane position downstream. It is considered that in the outer region of the flow field, the grid is relatively coarse and the fluctuation can happen when cut plane is crossing the cell boundaries.

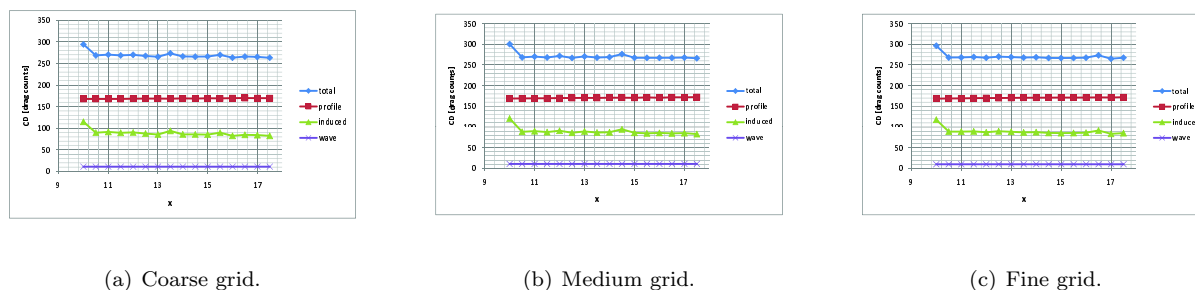


Figure 7. Drag variation versus cut-plane location.

C. Grid Convergence

The grid convergence characteristics which were got both from near-field and far-field analysis are shown in Fig. 8. In the figure, far-field drag computed using the computational field cut by the plane placed at $x = 11.0$ was employed. The far-field drag seems successfully removed the spurious drags and almost constant values from all the coarse, medium and fine grid within 2 drag counts. They are adequately close to the expected converted value of the near-field convergence study. The inconsistency for the fine grid was considered to be an influence of induced drag fluctuation. This induced drag fluctuation is mostly affecting on the final drag precision.

D. Profile drag polar

For the medium grid, the cases at the angles of attack of 1.5, 2.0, 2.5, 3.0 and 4.0 were also analysed with far-field analysis. Then, the profile drags plus wave drag calculated were overlapped with the idealized profile drag ($= C_D - C_L^2 / (\pi AR)$) of the DPW-4 results⁴ in Fig. 9. In the figure, orange line is the estimated far-field profile drag plus wave drag and the sky blue line is the value calculated from the JAXA near-field results.

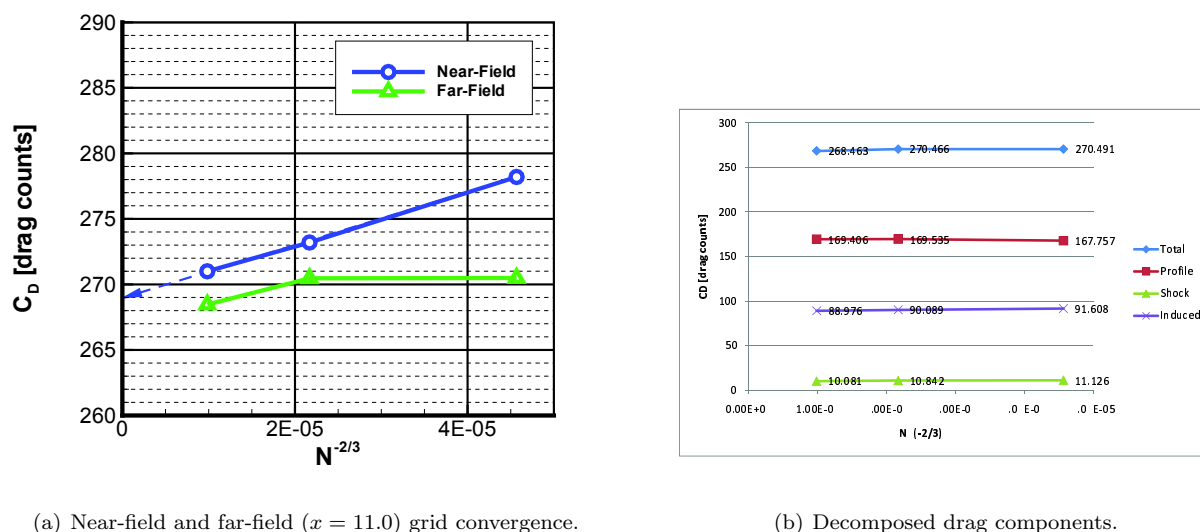


Figure 8. Grid convergence.

The profile drag calculated in far-field analysis has proper characteristics and it is almost lower limit of the variation of the DPW-4 results. The difference of the far-field and the near-field is almost same as the difference in Fig. 8(a). This means the difference in the idealized profile drag corresponds to the spurious drag itself. Therefore, the far-field drag curve in Fig. 9 would be expected to be closer to the converged one.

It is remarkable that most of the curves are steeply cranked over the $C_L = 0.6$. To examine the cause of it, decomposed drag components are examined and depicted in Fig. 10. The induced drag curve agree very well with the estimated idealized induced drag value. The wave drag curve and the profile drag curve are increasing at the higher C_L . It is to be noted that the profile drag curve is cranked at $C_L = 0.6$ and it gives the steepness to the drag curve.

To see the cause of this crank, visual inspection of profile drag production was performed. In Figs. 11, profile drag distributions are shown for the cases of $C_L = 0.5$ (Fig. 11(a)) and $\alpha = 4.0$ deg (Fig. 11(b)).

Corresponding to the wave drag increase in Fig. 10, increased drag production over the main wing is observed. An only remarkable profile drag difference should be a drag hump running out from the wing-body juncture. It is reported that in the solutions at higher angle of attack used in this analysis are estimating excess separation around the aft wing-body juncture, and an improvement with a non-linear model for turbulence models.¹⁶ Although the predictions for higher angle of attack showed large scattering of results in the DPW-4 due to this flow separation and it is under discussion in the workshop, the decomposed drag suggests that the boundary-layer separation on the wing is caused by a stronger shock wave. Therefore, the reliability of RANS predictions for this case probably depends on how they correctly predict shock induced boundary-layer separations at the wing-body juncture.

E. Spurious drag production

The results of grid convergence study using far-field analysis show that the far-field analysis can extract the spurious drag. To see where the spurious drag is occurring, spurious drag production was visualized in Fig. 12. In those figures, the gray cells represent boundary layer cells and the green cells are wave drag cells. Thus, the red cells are the cells producing the drag captured neither by boundary layer cells nor wave drag cells. They are the cells occurring spurious drag.

It is easily observed that the spurious drags are occurring around the leading edges of the main wing, horizontal tail and the nose area of the body.

To see the detail of the spurious drag production, entropy drag production images around the main wing were made at the span of $\eta = 0.5$ (Fig. 13). In the figure, the entropy drag production within the boundary layer and due to the shock on the aft-surface of the wing can be seen. To see the drag productions clearly, the colormap is set excessively emphasized. Then, the same figures are masked with the wave drag cells

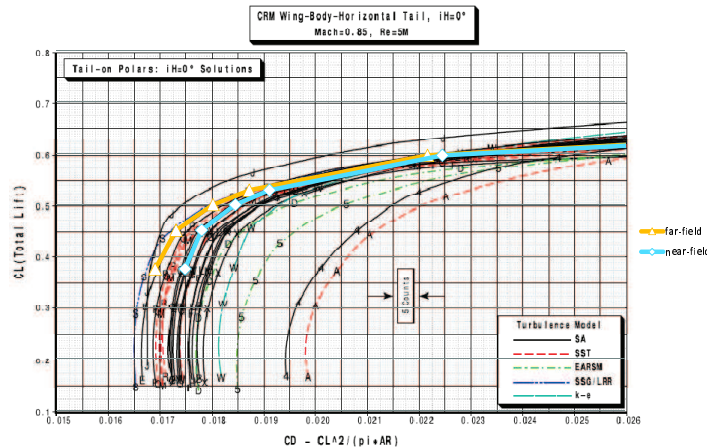


Figure 9. Idealized profile drag polars with DPW-4 results.

(green cells) and the boundary layer cells (gray cells) in Fig. 14. A chunk of spurious drag production is observed around the leading edge of the main wing and the strength of the spurious drag is decreasing with grid refinement. Additionally, pressure wave like drag production which are emitted from the leading edge to the upper flow field is seen. It should be spurious drag because it is decaying with the grid refinement. For the coarse grid, this pressure wave like drag production is almost reaching to the wave drag cells. It could affect the wave drag in a case of coarser grid and wave drag integration would be contaminated.

Around the leading edge of the super-critical wing, the air-flow is strongly accelerated and the velocity gradient from the no-slip wing wall to the accelerated flow and the flow curvature are also very strong. Even if the computational cells are concentrated around there, spurious drag for those cases are always occurring around the leading edge such as single cell is owing excessive entropy production.

V. Conclusions

Far-field drag analysis concerning the numerical simulation results of the NASA Common Research Model for the 4th AIAA drag prediction workshop performed by JAXA was conducted. Then, following conclusions were acquired:

- Even with the coarse grid, spurious drag is effectively removed and close value to the estimated converged drag for grid convergence study which is acquired in the near-field analysis.
- Comparison with the idealized drag polar curve from the DPW-4 results is reasonable.
- Decomposed drag components by far-field can reveal the drag production characteristics both quantitatively and qualitatively.
- Drag production visualization can give effective insight of the drag production.

Thus, it is shown quantitatively and qualitatively that the far-field analysis is promising method to analyse drag production in the flow-field acquired by computational fluid dynamics. At this moment, cell selection method both for wave drag and boundary layer is not perfect and geometrical margin setting is required. Advent of improved detection method would be expected.

Due to the increasing available computational resources, analyses using high quality and very dense grids are getting available and spurious drag might be less stringent in such cases. However, optimization loops or

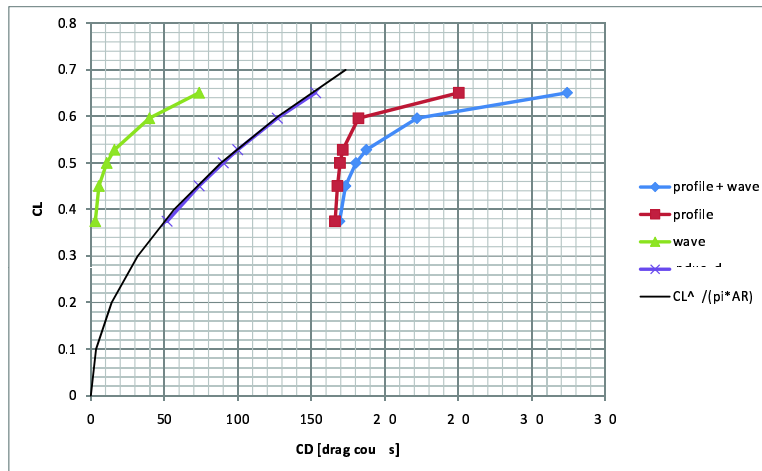
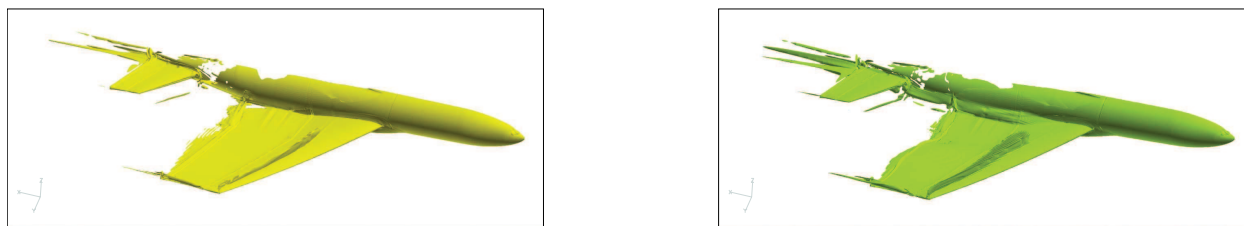
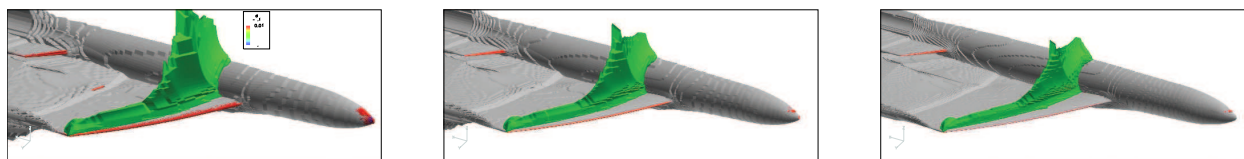


Figure 10. Decomposed drag polar.

development CFD campaigns require hundreds of flow computation and coarser grids are favorable in such cases. In addition, one of the important advantages of the far-field analysis is that the decomposed results guide us to what we could do in design concept and improvement to reduce fuel consumption.

References

- ¹Levy, D., Wahls, R., Zickuhr, T., Vassberg, J., Agrawal, S., Pirzadeh, S., and Hemsch, M., "Summary of Data from the First AIAA CFD Drag Prediction Workshop," AIAA Paper AIAA-2002-841, 40th AIAA Aerospace Sciences Meeting and Exhibit, Jan 2002.
- ²Laffin, K., Brodersen, O., Rakowitz, M., Vassberg, J., Wahls, R., Morrison, J., Tinoco, E., and Godard, J.-L., "Summary of Data from the Second AIAA CFD Drag Prediction Workshop," AIAA Paper AIAA-2004-555, 42nd AIAA Aerospace Sciences Meeting and Exhibit, Jan 2004.
- ³Vassberg, J., Tinoco, E., Mani, M., Brodersen, O., Eisfeld, B., Wahls, R., Morrison, J., Zickuhr, T., Laffin, K., and Mavriplis, D., "Summary of the Third AIAA CFD Drag Prediction Workshop," AIAA Paper AIAA-2007-260, 45th AIAA Aerospace Sciences Meeting and Exhibit, Jan 2007.
- ⁴Vassberg, J., Tinoco, E., Mani, M., Rider, B., Zickuhr, T., Levy, D., Brodersen, O., Eisfeld, B., Crippa, S., Wahls, R., Morrison, J., Mavriplis, D., and Murayama, M., "Summary of the Fourth AIAA CFD Drag Prediction Workshop," AIAA Paper AIAA-2010-4547, 28th AIAA Applied Aerodynamics Conference, Jan 2010.
- ⁵Morrison, J. H., "Statistical Analysis of CFD Solution from the Fourth AIAA Drag Prediction Workshop," AIAA Paper 2010-4673, 28th AIAA Applied Aerodynamics Conference, July 2010.
- ⁶van der Vooren, J. and Slooff, J., "CFD-Based Drag Prediction; State of the Art, Theory, Prospects," AIAA Professional Studies Series, Course on Drag-Prediction and Measurement TP 90247, NLR, 1990.
- ⁷van der Vooren, J. and Destarac, D., "Drag/thrust analysis of jet-propelled transonic transport aircraft: Definition of physical drag components," *Aerospace Science and Technology*, Vol. 8, No. 6, Sep 2004, pp. 545-556.
- ⁸Destarac, D., "Far-field / Near-field Drag Balance and Applications of Drag Extraction in CFD," *CFD-Based Aircraft Drag Prediction and Reduction*, VKI Lecture Series 2003-02, von Karman Institute for Fluid Dynamics, Belgium, Nov 2003.
- ⁹Tognaccini, R., "Methods for Drag Decomposition, Thrust-Drag Bookkeeping from CFD Calculations," *CFD-Based Aircraft Drag Prediction and Reduction*, VKI Lecture Series 2003-02, von Karman Institute for Fluid Dynamics, Belgium, Nov 2003.
- ¹⁰Yamazaki, W., Matsushima, K., and Kazuhiro, N., "Aerodynamic Design Optimization using the Drag-Decomposition Method," *AIAA Journal*, Vol. 46, May 2008, pp. 1096-1106.
- ¹¹Yamazaki, W., *Study of Advanced Aerodynamic Analysis & Shape Optimization Using Drag Decomposition Method*, Ph.D. thesis, Tohoku University, Jan 2007.
- ¹²Vos, J. B., Sanchi, S., and Gehri, A., "DPW4 Results Using Different Grids Including Near-Field/Far-Field Drag Analysis," AIAA Paper 2010-4552, 28th AIAA Applied Aerodynamics Conference, July 2010.

(a) $C_L = 0.5$ (b) $\alpha = 4.0\text{deg}$ **Figure 11. Profile drag differences between $C_L = 0.5$ and $\alpha = 4.0\text{deg}$** 

(a) Coarse.

(b) Medium.

(c) Fine.

Figure 12. Spurious drag production (red cells: spurious, white cells: boundary layer, green cells: shock).

¹³Maskell, E., "Progress Towards a Method for the Measurement of the Components of the Drag of a Wing of Finite Span," Tech. Rep. Technical Report 72232, RAE, 1972.

¹⁴Kusunose, K., *A Wake Integration Method for Airplane Drag Prediction*, Vol. 3 of *The 21st Century COE Program International COE of Flow Dynamics Lecture Series*, Tohoku University Press, Sendai, 2005.

¹⁵Eiji Shima, K. K. and Fujimoto, K., "New Gradient Calculation Method for MUSCL Type CFD Schemes in Arbitrary Polyhedra," AIAA Paper 2910-1081, Jan. 2010, In 48th AIAA Aerospace Sciences Meeting.

¹⁶Yamamoto, K., Tanaka, K., and Murayama, M., "Comparison Study of Drag Prediction for the 4th CFD Drag Prediction Workshop using Structured and Unstructured Mesh Methods," AIAA Paper 2010-4222, 28th AIAA Applied Aerodynamics Conference, June 2010.

¹⁷Takaki, R., Yamamoto, K., Yamane, T., Enomoto, S., and Mukai, J., "The Development of the UPACS CFD Environment," *Proceedings of ISHPC 2003*, High Performance Computing, Springer, 2003, pp. 307-319.

¹⁸Yamamoto, K., Ochi, A., Shima, E., and Takaki, R., "CFD Sensitivity of Drag Prediction on DLR-F6 Configuration by Structured Method and Unstructured Method," AIAA Paper AIAA-2004-398, 42nd AIAA Aerospace Sciences Meeting and Exhibit, Jan 2004.

¹⁹Roe, P., "Approximate Riemann Solvers, Parameter Vectors, and Difference Schemes," *Journal of Computational Physics*, Vol. 43, 1981, pp. 57-372.

²⁰van Albada, G., van Leer, B., and Jr., W. R., "A Comparative Study of Computational Methods in Cosmic Gas Dynamics," *Astronomy and Astrophysics*, Vol. 108, 1982, pp. 76-84.

²¹Shima, E., "A Simple Implicit Scheme for Structured/Unstructured CFD," *Proceedings of 29th Fluid Dynamics symposium*, Hokkaido, Japan, 1997, pp. 325-328.

²²Spalart, P. and Allmaras, S., "A One-Equation Turbulence Model for Aerodynamic Flows," Tech. Rep. AIAA 92-0439, 30th Aerospace Sciences Meeting and Exhibit, Reno, NV, Jan 6-9 1992.

²³AIAA, "CFD General Notation System," <http://cgns.sourceforge.net/>.

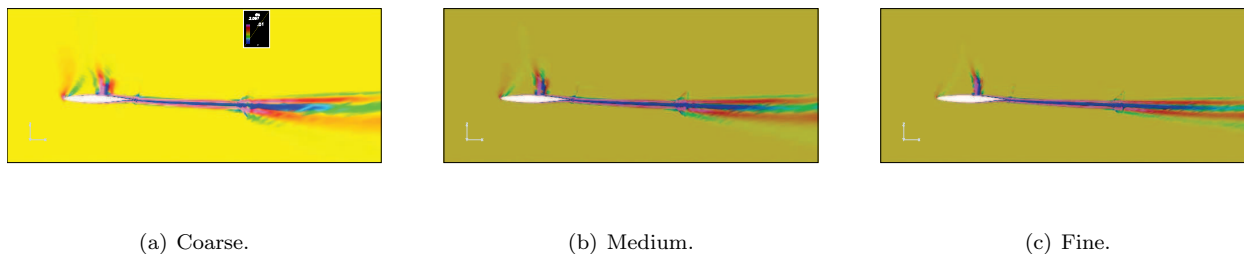


Figure 13. Entropy drag production around the airfoil at $\eta = 0.5$ (white cells: boundary layer, green cells: shock).

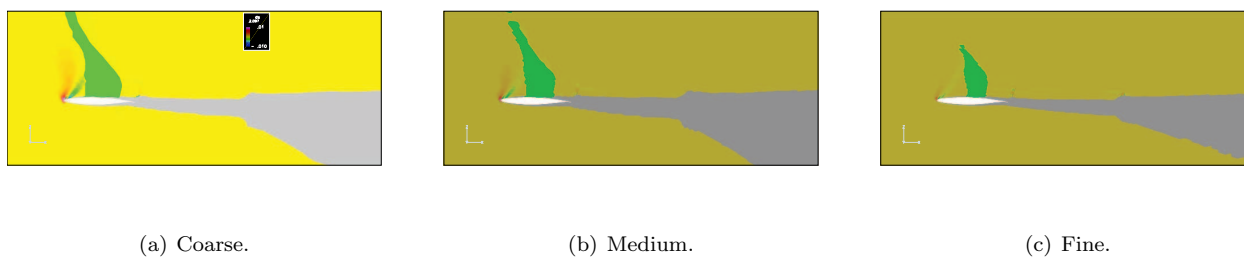


Figure 14. Spurious drag production around the airfoil at $\eta = 0.5$ (white cells: boundary layer, green cells: shock).